

# Determination of Geothermal Anomalies Through Multivariate Regression of Background Variables at Yellowstone National Park Using Landsat 5 TM Thermal Band Data

Sita Karki<sup>1</sup>, Shannon Kobs Nawotniak<sup>1</sup>, H. Carrie Bottenberg<sup>1</sup>, Michael McCurry<sup>1</sup>, and John Welhan<sup>1,2</sup>

<sup>1</sup>Department of Geosciences, Idaho State University, Pocatello ID

<sup>2</sup>Idaho Geological Survey, Idaho State University, Pocatello ID

[kobssh@isu.edu](mailto:kobssh@isu.edu)

## Keywords

*Landsat 5 TM, Yellowstone National Park, remote sensing, background subtraction, geothermal anomalies*

## ABSTRACT

Geothermal anomalies of Yellowstone National Park (YNP) are identified and quantified using Landsat 5 TM thermal band data. Multivariate regression of independent background variables that effect thermal emissivity, including elevation, slope, aspect, insolation, vegetation, water, soil moisture, and exposed land, were utilized in this study to create a comprehensive background filter for the raw imagery. Subtracting the multivariate background model from raw Landsat 5 TM data accentuates large geothermal anomalies such as Grand Prismatic and less thermally evident features such as the Old Faithful Geyser while removing significant false anomalies from the imagery. Geothermal anomaly emittances within YNP were calculated with a range of 40-120 W/m<sup>2</sup>. False positives for geothermal activity were reduced in the scene, with remaining ones focused on bare earth slope, consistent with other studies. A differencing between known geothermal pool temperatures and model residual temperatures at 25 sites indicates an average difference of 347 K (stdev 12 K), suggesting scalability from residual output to corrected temperature detection. The methodology employed for detecting known geothermal anomalies in YNP could be utilized to detect unknown geothermal potential in underexplored geothermal regions.

## 1. Introduction

All objects on the earth's surface emit electromagnetic radiation, which can be detected and measured using low-cost remote sensing techniques. Problematically, the raw emittance measured from satellite imagery includes the response from the target of interest as well as background or intervening features, which results in noise that can mask true anomalies. It is critical to differentiate signal sources when quantifying a specific thermal feature. In this work, we develop a multivariate background emittance model

that we use as a filter for Landsat TM data across Yellowstone National Park (YNP).

YNP is one of the most geothermally active and well-studied locations in the world, allowing us to validate our model against established records of geothermal anomalies of varying scale. Yellowstone is a large caldera in Wyoming, Montana, and Idaho, located at the western extent of the Snake River Plain. The volcano that last erupted cataclysmically 640Ka, depositing the >1000 km<sup>3</sup> Lava Creek Tuff, an event that was followed by smaller effusive eruptions as recently as 70Ka (Christiansen and Blank, 1972). The magmatic system underlying Yellowstone caldera remains active, as evidenced by continued passive degassing and ground deformation (e.g., Aly and Cochran, 2011). Faults and fractures in the crust in YNP provide pathways for water circulation from the surface to deep, relatively hot crust (Morgan et al., 1977; Bargar, 1978). This hydrothermal circulation manifests itself at the surface as geysers, mud pots, hot springs, and fumaroles; there are over 10,000 surficial geothermal anomalies within the park boundaries, with scales spanning centimeters to 10's of meters and temperatures up to the boiling point of water.

Despite the presence of such significant geothermal anomalies, thermal remote sensing analyses of the features have been hampered by noise from background emittance. Previous work by Coolbaugh et al. (2006) and Eneva et al. (2006) at YNP attempt to mitigate the noise problem in satellite-based remote sensing imagery by subtracting heat due to topography, thermal inertia and albedo. Similarly, Watson et al. (2008) calculated the geothermal emittance anomalies of YNP by correcting for solar and elevation effects using a snow covered Landsat 7 ETM+ scene to mask out other variables that emit thermal energy. While these approaches improve isolation of true positive thermal anomalies in satellite data, their success was limited by their *a priori* selection of a limited suite of contributing background variables. Following a different approach to noise filtering, Vaughan et al. (2012a and 2012b) calculated corrected net heat flux at known geothermal sites in YNP by subtracting heat from nearby non-geothermal areas. While this approach yielded excellent results, the method is inherently limited to use in areas of pre-defined, known anomalies from which the user can identify targets of interest and appropriate

neighboring non-geothermal pixels for subtraction. These limitations are problematic given the impact of geothermal anomalies on their surrounding conditions; for instance, elevated geothermal emittance can be very damaging to local vegetative health, which, in turn, influences overall thermal emittance as measured via remote sensing (Mia et al., 2012).

In this work, we evaluate the relative contributions of slope, aspect, elevation, vegetation, soil, and water to thermal emittance in geothermally inactive areas surrounding YNP to establish coefficient ranges appropriate for multivariate analysis. Minimum and maximum coefficients for each of the significant background variables define the solution bounds used in a Monte Carlo-based background filter for thermal anomalies within YNP boundaries. By defining coefficient ranges using non-geothermal zones, we reduce the risk of overfitting the algorithm for the thermal areas, thereby yielding false negatives in the final image.

## 2. Materials and Methods

We focused our study in and around YNP in northwestern Wyoming, eastern Idaho and southern Montana (Fig. 1). Training zones A through J represent areas similar to those within YNP but geothermally cold, as determined using data from the Idaho Department of Water Resources and Derkey and Johnson (1995). Diverse land conditions, such as steep slopes, vegetated areas and barren lands, were included to ensure model accommodation to wide range of environmental variability typical of the region. The independent variables were evaluated in the training areas in order to minimize overfitting of the model to the geothermal anomalies present inside YNP.

We used Landsat 5 TM satellite imagery (30 m spatial resolution, thermal resampled from 120 m), with imagery from

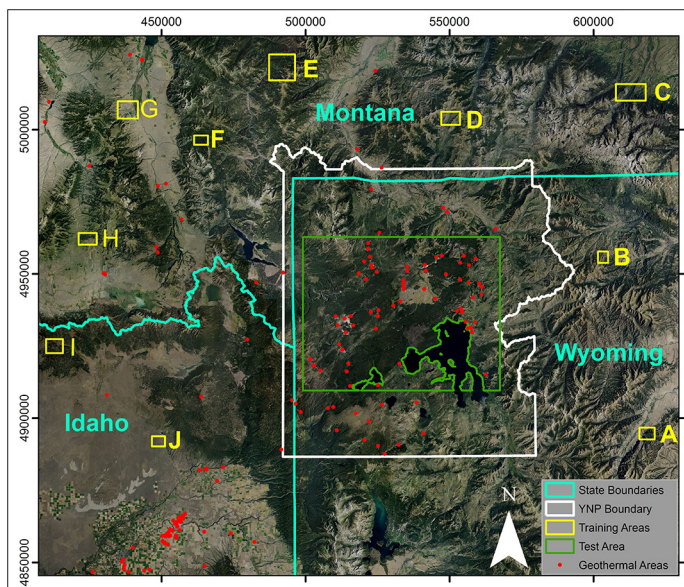


**Figure 1.** Map showing training areas (A to J; yellow boxes) around YNP (white outline) and test area (green outline) inside YNP. The red dots represent known geothermal anomalies. Points within the park boundary are from the polygons of R. Hutchinson (unpublished), points in Idaho are from Idaho Department of Water Resources (2001), points in Montana are from Derkey and Johnson (1995). Background image from NAIP 2012/13 Image Services.

September 24, 2011. The selected image did not contain snow or cloud cover, and was chosen to be outside of peak vegetation conditions; results from this image are consistent with output generated in August and October dates in other years. Although Landsat 7 ETM+ has 60 m resolution in the thermal infrared bands, we did not use this sensor due to technical problems associated with it since 2003 (Sobrino et al., 2008).

We examined elevation, slope, aspect, insolation, vegetation, water, soil moisture, and exposed land as independent variables to calculate the background emission via multivariate regression. The primary datasets used for calculating these derived variables were Landsat 5 TM imagery and National Elevation Datasets (NED). The Landsat 5 TM data were converted to radiance and temperature (for band 6) in ENVI software using standard calibration parameters (NASA, 2007; Chander et al., 2009).

Normalized Difference Vegetation Index (NDVI) was used to measure vegetation greenness, a proxy for vegetation health and plant type from Landsat 5 TM imagery. NDVI values range from 1 to -1, with higher values representing more greenness. Near infrared (NIR) and red bands were used to calculate NDVI using the equation (Jensen, 1986):

$$NDVI = \frac{NIR - red}{NIR + red} \quad (1)$$

The Normalized Difference Bare Soil Index (NDBSI) uses Shortwave Infrared (SWIR) and NIR bands to measure bare soil area and it is expressed as (Roy et al., 1997):

$$NDBSI = \frac{SWIR - NIR}{SWIR + NIR} \quad (2)$$

NDWI, or Normalized Difference Water Index (NDWI) is used to delineate water features and enhance its presence in remotely sensed imagery (McFeeters, 1996). The equation for NDWI is given as:

$$NDWI = \frac{green - NIR}{green + NIR} \quad (3)$$

We also calculated the *modified*-NDWI, which suppresses the noise from built-up land, soil and vegetation because of the use of SWIR instead of NIR (Xu, 2006). We included both indices at the outset of the study rather than making a priori decision regarding which would be more useful in the multivariate thermal algorithm; variables were evaluated for redundancy and significance before being included in the final model. The equation for *modified*-NDWI is given as:

$$modifiedNDWI = \frac{green - SWIR}{green + SWIR} \quad (4)$$

National Elevation Datasets (NED; 10 m spatial resolution) were used to calculate slope, aspect, hillshade and insolation in ArcGIS. Slope is the rate of change of elevation with distance, ranging from 0 to 90 degrees above horizontal. Aspect, or the direction of that the local slope is facing, is recorded as azimuthal compass direction. Hillshade is a function of solar azimuth and elevation. This study used the metadata associated with the corresponding Landsat image to calculate the hillshade for the day of the year and time of day the scene was collected. Slope, aspect and hillshade were calculated using the algorithms by Burrough

et al. (1998) native to ArcMap 10. Insolation, or solar radiation, was calculated using the hemispherical viewshed algorithm introduced by Rich et al. (1994) and developed by Fu and Rich (2000, 2002); the Area Solar Radiation tool in ArcMap 10 was used to calculate the insolation in Watt-hour/meter<sup>2</sup> at the time of day corresponding to the relevant Landsat image capture. Because date- and time-appropriate sun orientation was used in both the hillshade and insolation calculations, these variables are analogous to one another through they exist on different scales and use different units.

We used univariate regression to establish the significance of the potential background variables on the total emittance, retaining significant variables for use in the multivariate calculation (Fig. 2). A *p*-test with 95% confidence identified background variables that do not significantly contribute to the total emittance; variables that failed the *p*-test for more than half of the training areas were removed from further evaluation in the study.

Independent variables were evaluated for multicollinearity, or variable redundancy. NDWI and *modified*-NDWI, for instance, are similar approaches to measuring vegetation greenness; while those terms will clearly exhibit multicollinearity, other relationships between independent variables may be less clear. To test for multi-

collinearity, variables were combined into groups for multivariate analysis in ArcMap 10. Variable groups were built sequentially, adding one variable at a time, with Ordinary Least Squares (OLS) used to identify improved coefficient fits. Variance Inflation Factor (VIF) values determined from best-fit solutions indicated which variables demonstrated multicollinearity (O'Brien, 2007). In cases of redundancy, the variable with the highest coefficient of determination was preserved while the others were excluded from further analysis. NDVI, NDWI, and *modified*-NDWI tested positive for redundancy relative to one another, with NDVI retained. Similarly, insolation and hillshade were redundant to one another; inclusion of hillshade resulted in better model fit, so insolation was dropped from further analysis. In both cases of multicollinearity, removal of the redundant variable(s) did not have a significant effect on the overall coefficient of determination.

The univariate best-fit coefficients in the training zones for the remaining variables were used to create upper and lower bounds in the multivariate solution for YNP. By establishing coefficient bounds in geothermally cold but otherwise consistent zones, we restricted the degree to which the multivariate solution can overfit the geothermally active park. We did not use any predetermined weighting in selecting the coefficient ranges, as that would



**Figure 2.** Figure showing the R-squared values corresponding to each background variables. Slope, elevation and NDVI have lower R-squared values than rest of the variables. NDBSI and shaded relief has the biggest influence on the total emittance as demonstrated by the color.

prejudice the model toward one set of land conditions over another. Large, cold water bodies were excluded from the final analysis, however, as they would otherwise force the model to preferentially fit to them rather than the targeted terrestrial sites. The multivariate model used a Monte Carlo approach to coefficient selection within the established bounds. Given the size of YNP and the number of iterations necessary to converge on a stable solution, the multivariate solution was calculated using Fortran90 code with openMP for thread-scale parallelism. The resulting best-fit solution, which describes the background temperature, is subtracted from the original raw image to leave a residual that highlights the geothermal anomalies in YNP (Fig. 3). The residual image is converted to emittance from degrees Kelvin using the Stefan-Boltzmann equation.

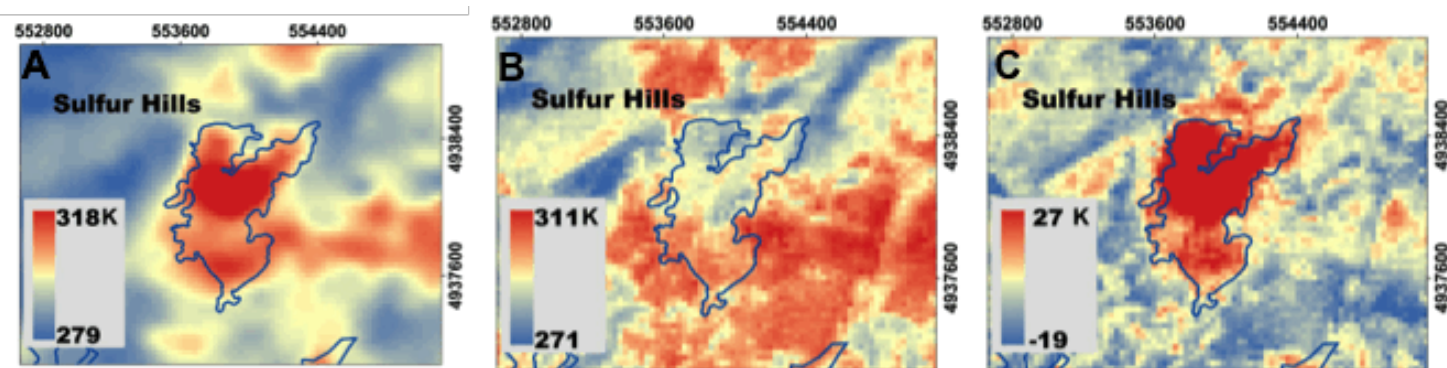


**Figure 3.** Close-up of the Sulfur-Hills Thermal-Area in YNP showing a) the raw Landsat 5 TM, b) multivariate background calculation, and c) residual (raw-background) images expressed in temperature (K). The blue polygons in the images are mapped geothermal zones by Hutchinson (unpublished). Subtracting the background from the raw image significantly highlights the geothermal anomaly relative to the false positive visible on the right side of the raw image. Location within YNP denoted on Figure 4; final output for Sulfur Hills in Figure 5e.

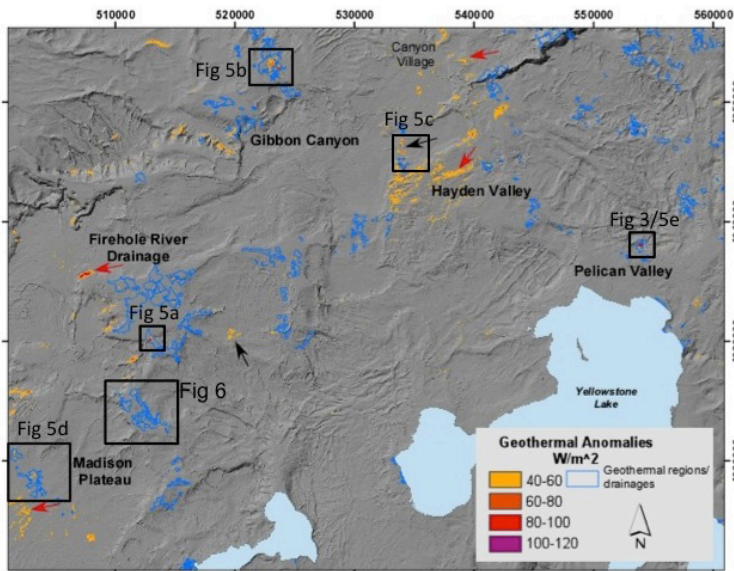


**Figure 4.** Residual emittance in YNP showing pixels greater than 3 standard deviations above the average for the zone. Blue polygons indicate geothermal zones as mapped by R. Hutchinson (unpublished). Red arrows indicate false anomalies in the image, while purple arrows denote positive identification of true anomalies consistent with ground truthing reports by Watson et al. (2008). False positives are preferentially located along northeast-trending ridges. Due to the scale of the test zone, presented here in overview, many of the positively identified thermal anomalies are not clearly visible in this image; see Figures 5 and 6 for closer views of anomalies.

The residual image produced by this method contains significant low-level background noise in addition to the emphasized thermal anomaly. This noise is minimized by removing all pixels with values less than 3 standard deviations above the average emittance, leaving only large anomalies. This filter approach can only be applied in circumstances where there are a large number of regular pixels relative to geothermally anomalous pixels, such as the park-wide analysis.

### 3. Results and Discussion

Application of the multivariate background model and 3 standard deviation filters results in very good agreement between modeled anomalies and field-evaluated geothermal anomalies across the park (Fig. 4). False anomalies occur in the output, mostly concentrated along northeast-trending ridges, as well as true anomalies that are not represented in the YNP polygon data but have been confirmed by Watson et al. (2008). The false anomalies that appear in the model output suggest that one of the variables may be underfitting the solution in certain circumstances, perhaps as a result of complex interplay between two or more variables, or that there may be a significant variable yet excluded from the analysis. Future work in this direction should include investigation of rock unit exposures, as they may be responsible for locally increased emittance.

The approach yielded particularly good fits with individual geothermal features within the anomaly polygons of R. Hutchinson (unpublished), available from the Yellowstone Center for Resources GIS geodatabase (Fig. 5). For example, the model distinguished between Grand Prismatic Spring and Excelsior Geyser Crater in the Midway Geyser Basin while minimizing the surrounding runoff zones in the polygon. Similarly, the model identified individual anomalies at the Violet Hot Springs, including both spring and mud pot features, and various geysers and pools in the Norris Geyser Basin. While large hot springs are most readily visible in the residual imagery, terrestrial anomalies with relatively small footprints are also identifiable;

Old Faithful and several other individual geysers are distinguishable from the background in the Upper Geyser Basin though it appears cold in the park-scale view (Fig. 6). The close-up perspective also shows some park infrastructure, such as

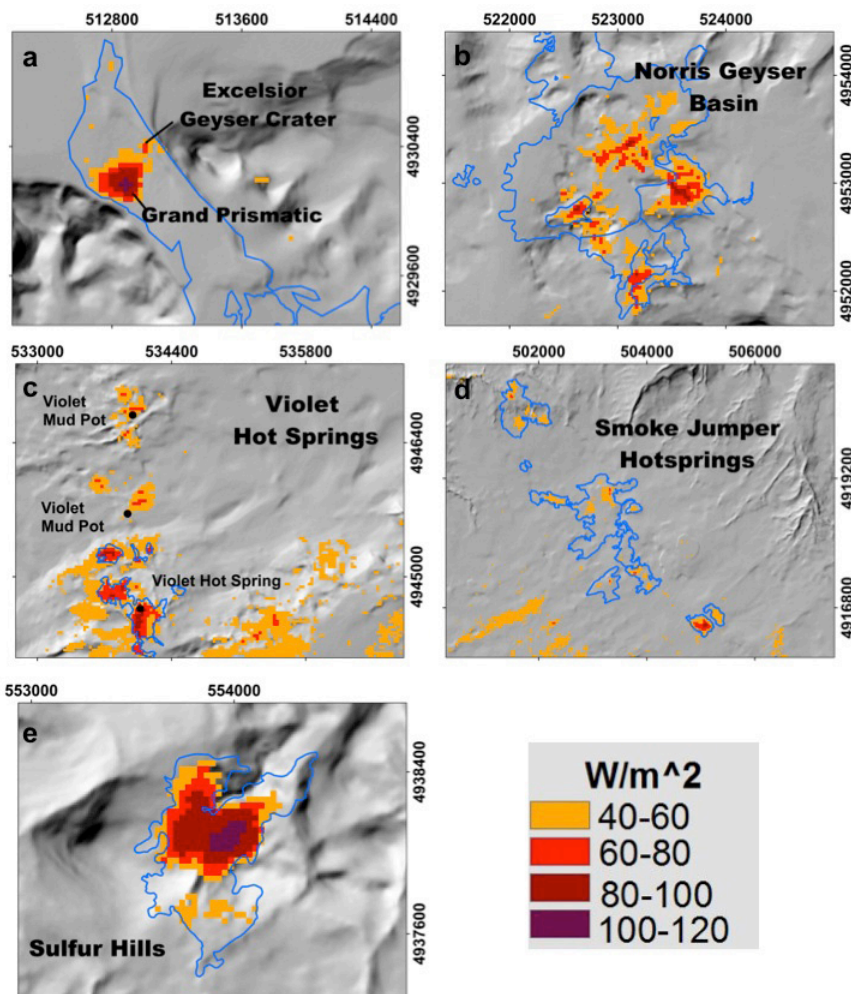


**Figure 5.** Close-up images of residual emittance for several geothermal anomalies in YNP. Features highlighted by the background filter model include hot spring pools, mud pots, and geysers. The method highlights the features within the broader mapped geothermal zones denoted by the blue polygons (R. Hutchinson, unpublished). Locations within YNP are denoted on Figure 4.

buildings and parking lots, as positive anomalies just above the display threshold (Fig. 6).

By subtracting background values in order to highlight true anomalies this model unavoidably reduces the output temperature to degrees in excess of background rather than real temperature. Twenty-five field temperature measurements of YNP pools by Bergfeld et al. (2011) were compared with spatially coincident model output to determine if there was a baseline offset that could be applied to the residual model pixels to convert them to true temperatures (Table 1). For the imagery presented here, the average difference between measured and modeled temperatures was 347 K, with a standard deviation of 12 K. Given the reported variability of YNP geothermal features over time (e.g., Friedman and Norton, 1981; Vaughan et al., 2012a; Savage et al., 2012) and signal mixing in coarse Landsat 5 TM 120 m pixels, this is a narrow distribution of differences. Evaluation of imagery from other dates will be necessary to establish whether this coarse scaling change

**Table 1.** Comparison points between measured field temperatures (Berfeld et al., 2011) and residual temperature from this model. This table indicates an average baseline temperature of 347 K offsetting residual from measured temperatures in the processed image. Note: field measurements occurred during Augusts and Septembers during the years 2003-2009 and do not indicate fluctuations that may have occurred during that period.

Location	Easting	Northing	Field Temp (K)	Residual Temp (K)	Difference (K)
Back Basin 2	522963	4952193	340.4	5.1	335.3
Back Basin 4	523011	4952171	360.4	7.5	352.9
Bear Creek	558816	4932859	365.3	10.0	355.3
Behind Congress	523655	4952727	365.7	7.5	358.2
Black Pit	523588	4952139	355.3	1.7	353.6
Black Sands 1	511542	4923259	363	10.2	352.8
Black Sands 2	511628	4923190	349.1	3.1	346.0
Chocolate Pots	520496	4950780	325.5	2.6	322.9
Dishwater	523384	4952086	362.4	5.4	357.0
Green Dragon	523196	4951898	361.6	7.5	354.1
Hot Springs Basin 2	558553	4953761	364.9	2.0	362.9
Hot Springs Basin 5	558925	4955398	349.9	5.0	344.9
Hot Springs Basin 8	559347	4954788	341.1	8.2	332.9
Hundred Springs Plain	523113	4953330	362.1	3.5	358.6
NR Gibbon R1	523658	4954007	357	0.5	356.5
NR Gibbon R2	523680	4954101	345.8	4.5	341.3
Obsidian Pool	544530	4939794	362.2	5.2	357.0
Potts Basin 1	533421	4919761	341.8	1.0	340.8
Potts Basin 2	533505	4919689	360.5	-0.3	360.8
Potts Basin 3	533504	4919547	318.3	-5.0	323.3
Smokejumper 1	503793	4917530	358	12.2	345.8
Steam Valve	523494	4952561	341.8	2.4	339.4
Sulphur Caldron 1	544992	4941758	341.9	3.7	338.2
Terrace Springs	512184	4944102	336.3	10.0	326.3
W Nymph Lake Thermal Area 1	520335	4954609	355	4.9	350.1

is broadly appropriate or is strongly influenced by intermediate diurnal and seasonal effects.

The background subtraction and 3 standard deviation pixel filter approaches used in this research pose a challenge for identifying relatively low-temperature thermal anomalies or anomalies with spatial footprints well under Landsat 5 TM pixel resolution. Comparing Figure 3c and Figure 5e, both of Sulfur Hills, illustrates the loss of low-grade thermal anomalies during the 3 standard deviation pixel filter used to minimize the visual impact of residual noise and low-confidence anomaly pixels. Further work will clarify the lower temperature and spatial limits of use for this model.

The ability of the method to identify relatively small spatial features despite the coarse pixel size available for thermal data through Landsat 5 TM suggests that the approach is worth investigating at higher resolution scales, such as the 1m resolution Forward Looking Infrared (FLIR) surveys used by Jaworowski et al. (2010). In their work, Jaworowski et al. (2010) identified significant relationships between park infrastructure and geothermal anomalies, with road construction resulting in diverted hydrothermal runoff and elevated temperatures on pavement. This interaction, located outside of mapped geothermal polygons, is also visible in our results as an anomaly located directly northeast of the Overpass Group (Fig. 6). Their high-resolution imagery was able to capture features below the visible threshold in this study, including the Circle Pool group approximately 500 m southeast of Grand Prismatic Spring.

In contrast to the approach of Vaughan et al. (2012a and 2012b), which was designed for monitoring changes in YNP heat flux, this method does not require *a priori* knowledge of geothermal anomalies and immediately proximal quiescent areas. As such, it can be more rapidly deployed as an exploratory tool over large areas. As presented, application of our proposed model

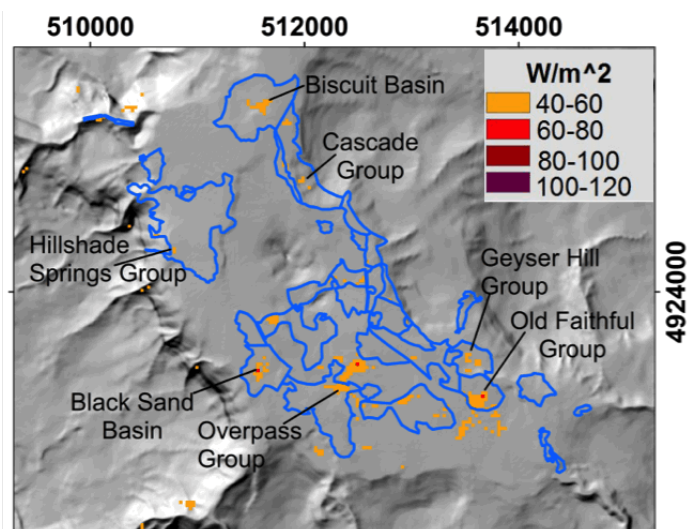


**Figure 6.** Upper Geyser Basin of YNP. Though the anomalies are indistinct when viewed at the park-wide scale in Figure 4, closer inspection of the Upper Geyser Basin reveals that the method discussed here identifies individual geysers within the group, including Old Faithful. Orange dots south of the Old Faithful Group correspond to park infrastructure, including buildings and parking lots. Blue polygons indicate geothermal zones as mapped by R. Hutchinson (unpublished).

requires identification of similar zones that are geothermally quiet for model coefficient training. This may be sidestepped, however, by processing large areas in which geothermally anomalous pixels make up a very small fraction of the total image, relaxing coefficient bounds, and allowing more iterations to achieve a convergent solution. In such an untrained case, the overwhelming number of cold pixels should prevent overfitting of the background model to the actual geothermal anomalies; while conceptually sound, the untrained approach should be evaluated prior to extensive use.

Previous work by Vaughan et al. (2012a and 2012b) and Watson et al. (2008) use winter scenes in order to minimize the effects of intervening background emittance. While both clearly show the merits of this approach, their models are thereby limited in the regions in which they can be applied. While the multivariate background subtraction method presented here requires that more variables be constrained, it is accordingly more appropriate for use in areas without reliable winter snow accumulation.

#### 4. Conclusions

The multivariate background subtraction method used in this study identified geothermal anomalies in YNP at multiple scales, from individual geysers to large hot springs and extensive geothermal anomaly clusters. This study is unique in that it successfully used multivariate regression analysis of Landsat TM 5 thermal infrared data to identify geothermal anomalies by developing a filter based on thorough explanation of background variables during snow-free conditions. By moving away from more traditional snow-filtering approaches, this model can be trained for use in potential geothermal areas in areas without regular snow accumulation. Future work will involve testing the inclusion of a geologic variable in the multivariate regression and investigation of complex relationships between independent variables that may contribute to false anomaly detection along northeast-trending ridges. The model will also be tested in geothermally active regions outside of YNP to evaluate robustness in different climate zones, with a focus on minimizing time required for coefficient training. Results from the current model application in YNP suggest that it is a low-cost, solution for geothermal anomaly detection over large areas for both large- and small-scale features.

#### References

- Aly, M.H. and Cochran, E.S., 2011. Spatio-temporal evolution of Yellowstone deformation between 1992 and 2009 from InSAR and GPS observations. *Bulletin of Volcanology* 73(9), 1407-1419.
- Bargar, K.E., 1978. Geology and Thermal History of Mammoth Hot Springs, Yellowstone National Park, Wyoming. *Geological Survey Bulletin* 1444, 55p.
- Bergfeld, D., Lowenstern, J.B., Hunt, A.G., Shanks, W.C.P. III, and Evans, W.C., 2011. Gas and isotope chemistry of thermal features in Yellowstone National Park, Wyoming: U.S. Geological Survey Scientific Investigations Report 2011-5012, 26 p. and data files.
- Burrough, P. A., and McDonell, R. A., 1998. *Principles of Geographical Information Systems*, Oxford University Press, New York, 190p.
- Chander, G., Markham, B., and Helder, D. 2009. Summary of current radiometric calibration coefficients for Landsat MSS, TM, ETM+, and EO-1 ALI sensors. *Remote Sensing of the Environment*, 113, 893-903.
- Christiansen, R.L., and Blank Jr., H.R., 1972. Volcanic stratigraphy of the Quaternary rhyolite plateau in Yellowstone National Park. *United States Geological Survey Professional Paper* 729-B, 18p.
- Coolbaugh, M.F., Kratt, C., Fallacaro, A., Calvin, W.M. and Tranik, J.V., 2006. Detection of Geothermal Anomalies using Advanced Spaceborne Thermal Emission and Reflection Radiometer (ASTER) Thermal Infrared Images at Brady Hot Springs, Nevada, USA. *Remote Sensing of Environment*, 106, 350-359.
- Derkey, P.D., and Johnson, B.R., 1995. Digital Maps of Low- to Moderate-Temperature Geothermal Spring and Wells in the Pacific Northwest: A Contribution to the Interior Columbia Basin Ecosystem Management Project. *US Geological Survey Open-File Report* 95-689, 11p. [online] Available at: < <http://pubs.usgs.gov/of/1995/of95-689/> > [Accessed 20 October 2012].
- Eneva, M., Coolbaugh, M. and Combs, J., 2006. Application of Satellite Thermal Infrared Imagery to Geothermal Exploration in East Central California. *GRC Transactions*, 30, 407-412.
- Friedman, I. and Norton, D.R., 1981. Ground Temperature Measurements: Part III, Ground Temperatures in and near Yellowstone National Park. *United States Geological Survey Professional Paper* 120, 23-39.
- Fu, P., and Rich, P. M., 2000. *The Solar Analyst 1.0 Manual*. Helios Environmental Modeling Institute (HEMI), USA, 46p.
- Fu, P., and Rich, P. M., 2002. A Geometric Solar Radiation Model with Applications in Agriculture and Forestry. *Computers and Electronics in Agriculture* 37, 25-35.
- Idaho Department of Water Resources (IDWR), 2001. *Geothermal Resources*. [online] Available at: < <http://www.idwr.idaho.gov/GeographicInfo/GISdata/geothermal.htm> > [Accessed 20 October 2012].
- Jaworowski, C., Heasler, H.P., Neale, C.M.U., and Sivarajan, S., 2010. Using Thermal Infrared Imagery and LiDAR in Yellowstone Geyser Basins. *Yellowstone Science* 18(1), 8-19.
- Jensen, J. R., 1986. *Introductory Digital Image Processing*, Prentice-Hall, New Jersey, 379p.
- McFeeters, S.K., 1996. The use of the Normalized Difference Water Index (NDWI) in the Delineation of Open Water Features. *International Journal of Remote Sensing*, 17(7), 1425-1432.
- Mia, Md.B., Bromley, C.J., and Fujimitsu, Y., 2012. Monitoring heat flux using Landsat TM/ETM+ thermal infrared data- A case study at Karapiti ('Craters of the Moon') thermal area, New Zealand. *Journal of Volcanology and Geothermal Research*. 235-236, 1-10.
- Morgan, P., Blackwell, D.D., Spafford, R.E., Smith, R.B., 1977. Heat flow measurements in Yellowstone Lake and the thermal structure of Yellowstone Caldera. *Journal of Geophysical Research* 82(26), 3719-3732.
- National Aeronautics and Space Administration (NASA). *Landsat 7 Science Data Users Handbook*. Updated October 2007, [online] Available at: < [http://landsathandbook.gsfc.nasa.gov/pdfs/Landsat7\\_Handbook.pdf](http://landsathandbook.gsfc.nasa.gov/pdfs/Landsat7_Handbook.pdf) > [Accessed 20 November, 2012].
- O'Brien, R.M., 2007. A Caution Regarding Rules of Thumb for Variance Inflation Factors. *Quality and Quantity*, 41, 673-690.
- Rich, P., Dubayah, M.R., Hetrick, W.A., and Saving, S.C., 1994. Using Viewshed Models to Calculate Intercepted Solar Radiation: Applications in Ecology. *American Society for Photogrammetry and Remote Sensing Technical Papers*, 524-529.
- Roy, P.S., Miyatake, S. and Rikimaru, A., 1997. Biophysical Spectral Response Modeling Approach for Forest Density Stratification. *Proceedings of the 18<sup>th</sup> Asian Conference on Remote Sensing*, October 20-24, 1997, Malaysia. [Online]. Available at: < <http://www.a-a-r-s.org/aars/proceeding/ACRS1997/Papers/FR97-7.htm> >.
- Savage, S.L., Lawrence, R.L., Custer, S.G., Jewett J.T., Powell, S.L. and Shaw, J.A., 2012. Analyzing Change in Yellowstone's Terrestrial Emittance with Landsat Imagery. *GIScience & Remote Sensing*, 49(2), 317-345.

- Sobrino, J.A., Jiménez-Muñoz, J.C., Sòria, G., Romaguera, M. and Guanter, L., 2008. Land Surface Emissivity Retrieval from Different VNIR and TIR Sensors. *IEEE Transactions on Geoscience and Remote Sensing*, 46(2), 316-327.
- United States Department of Agriculture (USDA). *National Agriculture Imagery Program (NAIP)*. [ArcGIS Image Service] Available at: < <http://gis.apfo.usda.gov/arcgis/services> > [Accessed 10 Oct 2012].
- Vaughan, R.G., Keszthelyi, L.P., Lowenstern, J.B., Jaworowski, C. and Heasler, H., 2012a. Use of ASTER and MODIS Thermal Infrared Data to Quantify Heat Flow and Hydrothermal Change at Yellowstone National Park. *Journal of Volcanology and Geothermal Research*, 233–234, 72-89.
- Vaughan, R.G., Lowenstern, J.B., Keszthelyi, L.P., Jaworowski, C., and Heasler, H., 2012b. Mapping Temperature and Radiant Geothermal Heat Flux Anomalies in the Yellowstone Geothermal System Using ASTER Thermal Infrared Data. *GRC Transactions* 36, 1403-1410.
- Watson, R.G.R., Lockwood, R.E., Newman, W.B., Anderson, T.N. and Garrott, R.A., 2008. Development and Comparison of Landsat Radiometric and Snowpack Model Inversion Techniques for Estimating Geothermal Heat Flux. *Remote Sensing of Environment* 112, 471-481.
- Xu, H., 2006. Modification of Normalized Difference Water Index (NDWI) to Enhance Open Water Features in Remotely Sensed Imagery. *International Journal of Remote Sensing*, 27(14), 3025-3033.

